Desalination and Water Treatment
www.deswater.com

doi: 10.5004/dwt.2017.20533

71 (2017) 32–44
April

Theoretical and experimental studies of direct contact membrane distillation modules with inserting W-shaped carbon-fiber spacers

Chii-Dong Ho[a,*], Luke Chen[b], Jing-Yuan Lai[a], Choon Aun Ng[c]

[a]*Energy and Opto-Electronic Materials Research Center, Department of Chemical and Materials Engineering, Tamkang University, Tamsui, New Taipei 251, Taiwan, Tel. +886 2 26215656; Fax:+886 2 26209887; emails: cdho@mail.tku.edu.tw (C.D. Ho), peacehiop4ever@hotmail.com (J.Y. Lai)*
[b]*Department of Water Resources and Environmental Engineering Tamkang University, Tamsui, New Taipei 251, Taiwan, email: luke@mail.tku.edu.tw (L. Chen)*
[c]*Department of Environmental Engineering, FEGT, UTAR, Kampar, Malaysia, email: ngca@utar.edu.my (C.A. Ng)*

Received 30 September 2016; Accepted 19 January 2017

ABSTRACT

The modeling equations for predicting distillate flux in the flat-plate direct contact membrane distillation module with inserting W-shaped carbon-fiber spacers of various hydrodynamic angles in flow channels were developed theoretically and experimentally. The pure water productivity and temperature distributions of both hot and cold feed streams are represented graphically with the volumetric flow rate, inlet saline temperature as parameters, and the experimental data were incorporated with the slot opening of the spacers and hydrodynamic angle as parameters to validate the theoretical predictions. A description of the average Nusselt number was made to evolve a correlation for a heat transfer coefficient correction factor in incorporating with experimental data. The effects of operating and design parameters such as volumetric flow rate, slot opening and hydrodynamic angle of the spacers, and fluid inlet temperature on pure water productivity and production energy efficiency were also delineated.

Keywords: Membrane processes; Hydrodynamics; Desalination; Permeate flux; Temperature polarization; Thermal boundary layer

1. Introduction

In membrane distillation (MD) operations, the volatile species in the hot feed fluid vaporizes at a hydrophobic membrane surface and permeates through the membrane by the driving force of vapor pressure difference across the membrane [1], in which only water vapor molecules are transported across porous hydrophobic membranes resulting in the high purity water production [2]. The temperature polarization effect causes the reduction of thermal driving-force and transmembrane mass flux is thus reduced, as shown in Fig. 1. The desalination of dissolved salts has received a great deal of attention to produce portable water in remote villages or rural areas where drinking water is short and the advantages lie in its simplicity and low operating cost by using low grade thermal energy for producing pure water and developments of MD systems [3–5]. MD has been recognized as an economically feasible technology of its low operating temperature [6] and used widely in saline water desalination [7], waste water treatment [8], and juice concentration [9]. The advantages of membrane technology in desalination processes [10,11] are in its simplicity and the low energy demand. The direct contact membrane distillation (DCMD) device in this study is an MD module for which the hot saline stream and cold liquid directly contact on both membrane surfaces resulting in a vapor pressure difference to allow only the vapor transport across a hydrophobic porous membrane. The turbulence promoter such as filaments [12] was used to disturb the thermal boundary layer, and thus, the polarization effect was minimized accompanying with

* Corresponding author.

a permeate flux enhancement of pure water productivity. Moreover, the distillate flux enhancement was achieved by employing roughened-surface flow channels [13], which acts as barriers and leads to the penalty of the friction loss increment that results in more energy consumption. A new design with inserting W-shaped carbon-fiber spacers of various hydrodynamic angles in flow channels in the flat-plate DCMD module was developed theoretically and experimentally. Many previous investigations focused on the modeling of membrane performance [14,15]. The temperature polarization effect creates temperature gradients in the hot saline stream [16,17] due to the heat required to vaporize water at the membrane–liquid interface, while there is insufficient heat supply from hot bulk flow passing through thermal boundary layer to sustain the vaporization of water, and the permeate flux is thus decreased. Previous study had proved that various designs of hollow fiber membrane module with baffles, spacers, and modified hollow fiber geometries applied in DCMD could promote flux enhancement [18]. Some works have been done by using eddy promoter in flow channel [13,21] for reducing the temperature polarization effect and concluded with a favorable result to enhance the device permeate flux performance of MD operations. This approach has been employed to design improved DCMD modules with inserting W-shaped carbon-fiber spacers and to develop a mathematical model for predicting the pure water productivity. In this work, the device performance improvements were achieved and investigated experimentally and theoretically under both concurrent- and countercurrent-flow operations with various operation and design parameters. Utilizing the experimental results and the theoretical predictions, a correlated expression of the heat transfer enhancement with the design of the inserting carbon-fiber spacers was developed. The effect of W-shaped carbon-fiber spacers on the permeation flux, pure water productivity increment, and energy consumption increment were analyzed.

2. Theoretical model

The DCMD module with inserting a hydrophobic microporous membrane was constructed to conduct both concurrent- and countercurrent-flow operations in aiming to produce the distillate flux of pure water, as shown in Fig. 2. For DCMD system, a theoretical model considering both heat and mass transfer mechanisms to deepen understanding of the vapor molecules transported through porous hydrophobic membranes. The mass transfer occurs in the porous membrane and the cold permeate side while the heat transfer takes place in the domains including the hot-fluid side, membrane, and the cold permeate side of the distillation process, as shown in Fig. 1. The theoretical analysis is based on considering the following assumptions: (a) under steady-state operations; (b) physical properties of fluid, plates, and membrane are constants; (c) stagnant air within the membrane pore; (d) mass transfer by diffusion and heat transfer by conduction as well as latent heat associated with water evaporation; (e) no water passing through the membrane; and (f) well insulation on the bottom and edge sides of modules.

The non-isothermal process in DCMD module generates the transmembrane mass flux depends on the temperature difference across the system resulting in heat conduction and producing pure water, which is controlled by the boundary layer heat transfer of both fluid streams. The heat fluxes transferred across the thermal boundary layers to and from the membrane surfaces can be determined by convective heat transfer coefficients and expressed as:

$$q_h = h_h(T_h - T_2) \quad (1)$$

$$q_c = h_c(T_1 - T_c) \quad (2)$$

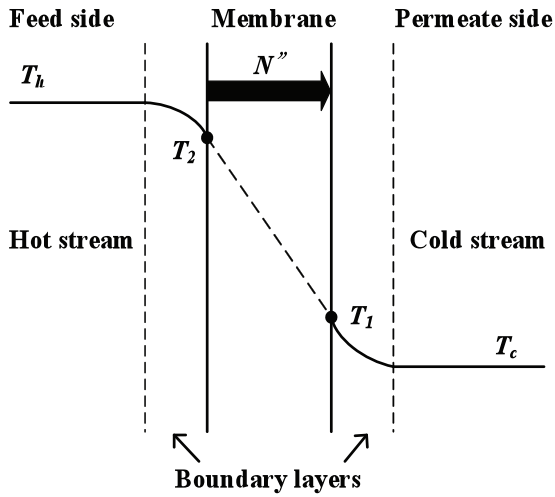

Fig. 1. Thermal boundary layers in a DCMD operation.

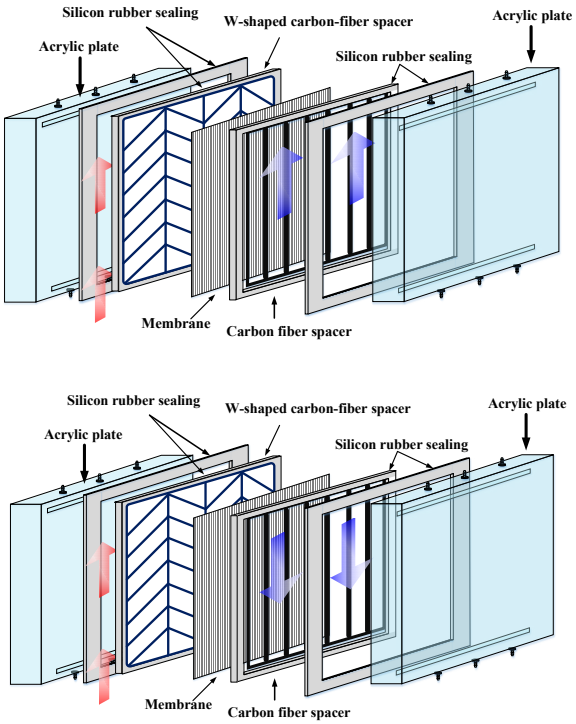

Fig. 2. Components of one unit of the DCMD module. (a) Concurrent-flow operations and (b) countercurrent-flow operations.

The temperature polarization coefficient (TPC), which is commonly used to express the significance of the fluid side heat transfer resistances, is defined as:

$$TPC = (T_2 - T_1)/(T_h - T_c) \tag{3}$$

A higher value of TPC represents smaller boundary layer resistances. The heat fluxes transferred across the thermal boundary layers to the membrane surfaces by using the convective heat-transfer coefficients, and the heat transferred through the membrane includes the latent heat associated with the permeate flux and the conductive heat transfer across the membrane can be expressed as:

$$q_m = N''\lambda + \frac{k_m}{\delta_m}(T_2 - T_1) \tag{4}$$

where the thermal conductivity of the membrane can be determined by the thermal conductivities of vapor in the membrane pore and the solid membrane material by [20]:

$$k_m = \varepsilon k_g + (1-\varepsilon)k_s \tag{5}$$

The modeling equations among the heat fluxes for all layers and for the one-dimensional bulk fluids with assuming well insulation on the bottom and edge sides of modules give:

$$q = q_h = q_m = q_c \tag{6}$$

The following equation can be used to express the amount of vapor flux that passes through the membrane pores incorporating with the energy balance of hot fluid and cold fluid gives:

$$\frac{dT_h}{dz} = \frac{-Wq}{Q\rho_h C_{ph}} \tag{7}$$

$$\frac{dT_c}{dz} = \frac{Wq}{Q\rho_c C_{pc}} \tag{8a}$$

$$\frac{dT_c}{dz} = \frac{-Wq}{Q\rho_c C_{pc}} \tag{8b}$$

where z is the flow direction of fluid. Eqs. (8a) and (8b) are for the concurrent- and countercurrent-flow operations, respectively. The mass transfer flux is determined by the consideration of the mass transfer resistances in series of the membrane and both fluid streams. The permeate transport across the membrane is due to the saturation vapor pressure difference caused by the temperature gradient on both membrane surfaces. The permeate flux of water vapor can be estimated using a membrane permeation coefficient c_m [21] and the transmembrane saturation vapor pressure difference ΔP to express the

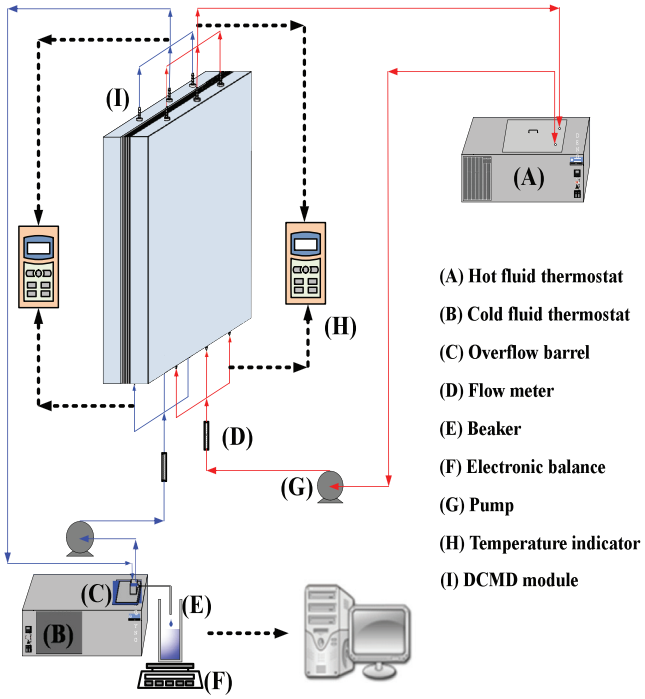

Fig. 3. Experimental setup for concurrent-flow operations.

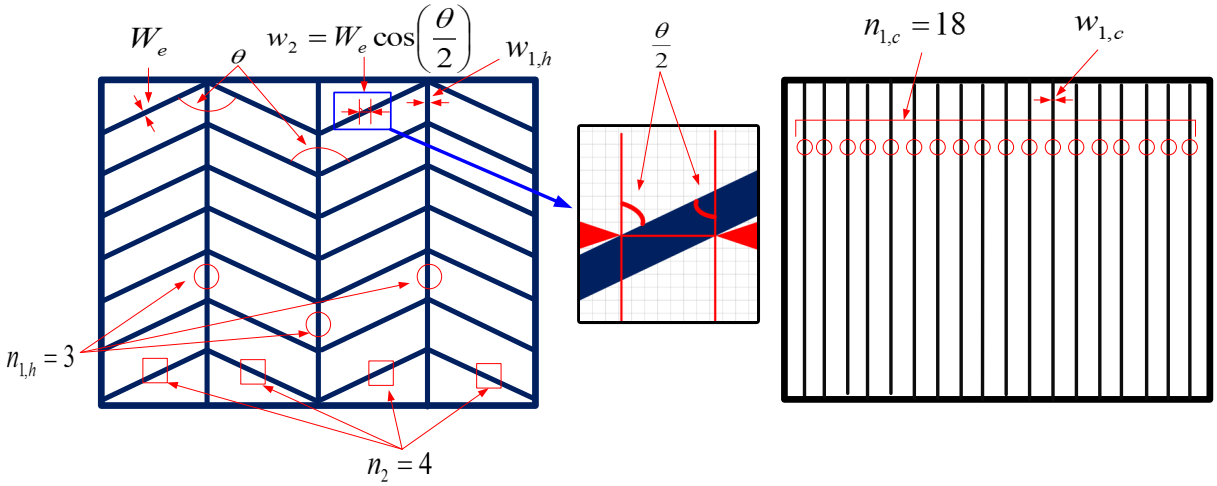

Fig. 4. Parameters of the inserted W-shaped carbon-fiber spacer.

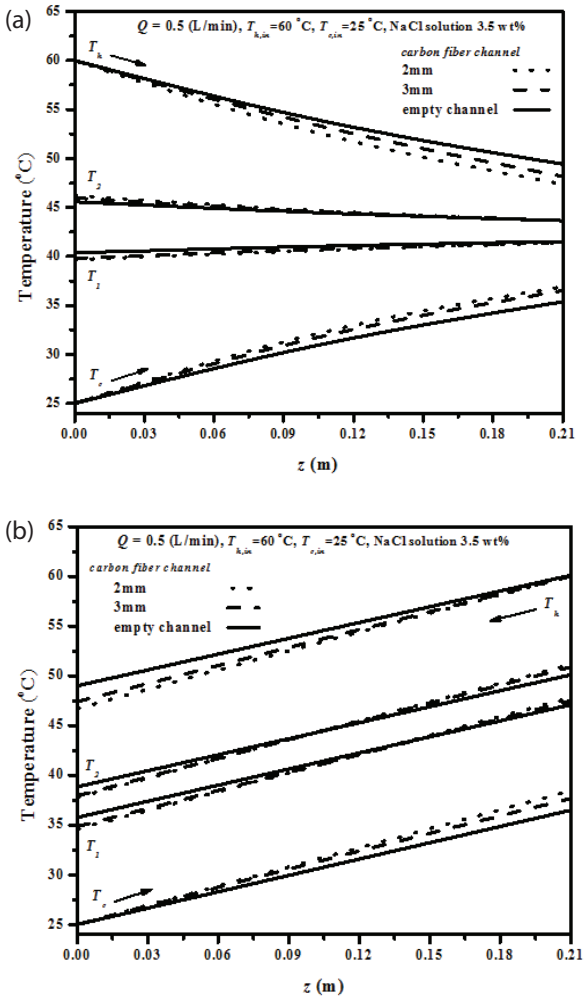

Fig. 5. Effect of the W-shaped carbon-fiber spacer design on temperature distributions. (a) Concurrent-flow operations and (b) countercurrent-flow operations.

Table 1(a)
The effect of channel design on temperature gradient across the membrane surfaces along the channel for concurrent-flow operation

z (m)	ΔT (°C)				
	Empty channel	2 mm	Increase (%)	3 mm	Increase (%)
0.06	4.04	4.87	20.5	4.61	14.0
0.12	3.11	3.57	15.0	3.40	9.4
0.18	2.39	2.63	10.2	2.53	5.8

amount of permeate flux that passes through the membrane pores as:

$$N'' = c_m \Delta P = c_m \left[P_2^{sat}(T_2) - P_1^{sat}(T_1) \right] \quad (9)$$

Table 1(b)
The effect of channel design on temperature gradient across the membrane surfaces along the channel for countercurrent-flow operation

z (m)	ΔT (°C)				
	Empty channel	2 mm	Increase (%)	3 mm	Increase (%)
0.06	3.05	3.64	19.4	3.56	16.73
0.12	3.04	3.55	16.8	3.43	12.96
0.18	3.02	3.47	14.9	3.31	9.38

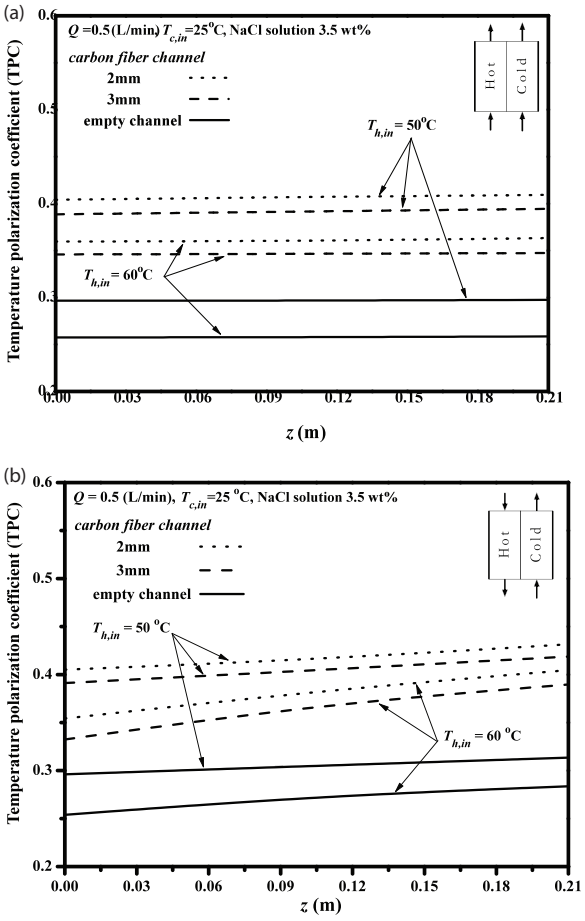

Fig. 6. Effect of inlet saline temperature, flow types and the W-shaped carbon-fiber spacer design on TPC. (a) Concurrent-flow operations and (b) countercurrent-flow operations.

where P_1^{sat} and P_2^{sat} are the saturated pressure of water vapor on the membrane surfaces in both hot saline stream and cold-fluid stream, and were calculated using the Antoine equation. The driving force across the membrane is the difference in saturated pressure on both membrane surfaces, and hence, the permeate flux diffuses through the membrane as the collected water condensate. The hot-fluid side saturation vapor pressure (P_2^{sat}) can be estimated using water activity coefficient (a_w), which can be determined by a correlation [10]:

$$P_2^{sat} = y_w P = x_w a_w P_w^{sat} \tag{10}$$

$$a_w = 1 - 0.5x_{NaCl} - 10x_{NaCl}^2 \tag{11}$$

Based on the mean free path of water molecule and the membrane pore size, Knudsen diffusion and molecular diffusion [10,22] are considered to determine the membrane permeation coefficient:

$$c_m = \left(\frac{1}{c_K} + \frac{1}{c_M}\right)^{-1} = \left\{\left[1.064\frac{\varepsilon r}{\tau\delta_m}\left(\frac{M_w}{RT_m}\right)^{1/2}\right]^{-1} + \left[\frac{1}{|Y_m|_{ln}}\frac{D_m\varepsilon}{\delta_m\tau}\frac{M_w}{RT_m}\right]^{-1}\right\}^{-1} \tag{12}$$

where the tortuosity (τ) can be estimated using the porosity of the membrane [22]:

$$\tau = \frac{1}{\varepsilon} \tag{13}$$

The temperatures of the hot fluid, cold fluid, and membrane interfaces along the length of the module as well as the permeate flux can be solved using fourth-order Runge–Kutta method with an iterative procedure to determine the convective heat transfer coefficients once the initial guess of the convective heat transfer coefficients is given. For heat transfer in channels without inserting carbon-fiber spacers (empty channel) under laminar flow, the commonly used correlation [23] is:

$$Nu_{lam} = 4.36 + \frac{0.036\,\mathrm{Re}\,\mathrm{Pr}\left(De/L\right)}{1 + 0.011\left(\mathrm{Re}\,\mathrm{Pr}\left(De/L\right)\right)^{0.8}} \tag{14}$$

The degree of heat transfer enhancement is commonly expressed by an enhancement factor, which is the ratio of the heat transfer coefficient of enhanced channel with inserting W-shaped carbon-fiber spacers to that of empty channel. The enhancement factor for heat transfer coefficient can be defined for DCMD modules using channels with W-shaped carbon-fiber spacers relative to empty channels.

$$Nu^E = \frac{hDe}{k} = \alpha^E Nu_{lam} \tag{15}$$

The Nusselt number of channels with inserting W-shaped carbon-fiber spacers can be related to five dimensionless groups according to Buckingham's π theorem:

$$Nu^E = f\left(\frac{W_e}{De_f}, \frac{L}{De_f}, \sin\theta, \mathrm{Re}, \mathrm{Pr}\right) \tag{16}$$

where W_e and L are fin width of carbon-fiber open slot separators and channel length, and De_f is the hydraulic diameter of the empty channel as illustrated in Fig. 4.

The energy consumption increment is inevitable due to the increased frictional loss with the inserting the W-shaped carbon-fiber spacers. The energy consumption of a DCMD module, which includes the contributions from the hot-fluid side and cold-fluid side, may be determined using Fanning friction factor f_F [24]:

$$P_{lost} = P_h + P_c = \dot{m}_h \ell w_{f,h} + \dot{m}_c \ell w_{f,c} = Q\rho_h \ell w_{f,h} + Q\rho_c \ell w_{f,c} \tag{17}$$

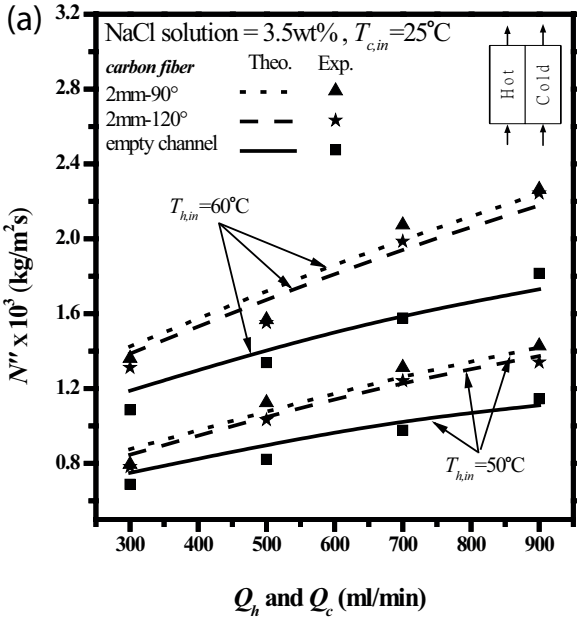

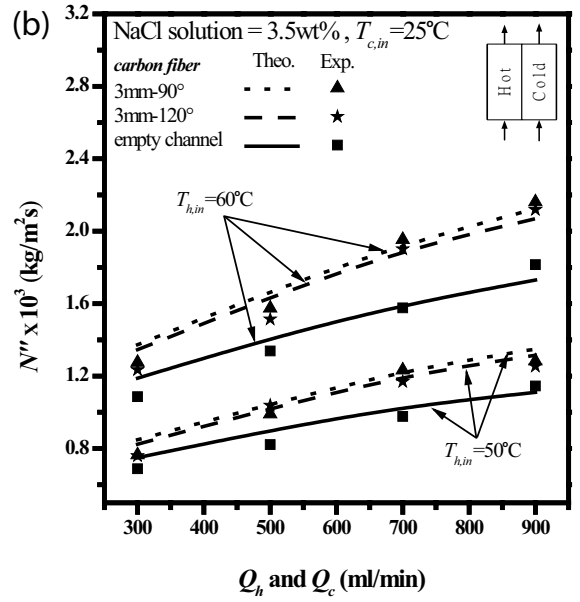

Fig. 7. Effect of hydrodynamic angle of the spacer and flow type on distillate flux. (a): (I) Effect of slot angle of the 2 mm W-shaped carbon-fiber spacer on distillate flux for concurrent-flow operations and (II) effect of slot angle of the 3 mm W-shaped carbon-fiber spacer on distillate flux for concurrent-flow operations.(b): (I) Effect of slot angle of the 2 mm W-shaped carbon-fiber spacer on distillate flux for countercurrent-flow operations and (II) effect of slot angle of the 3 mm W-shaped carbon-fiber spacer on distillate flux for countercurrent-flow operations.

Table 2(a)
Comparison of theoretical and experimental permeates flux of various operation conditions and channel design for concurrent-flow operations

$T_{h,in}$ (°C)	Q (L/min)	Empty channel			Carbon-fiber channel											
					2 mm, 90°			2 mm, 120°			3 mm, 90°			3 mm, 120°		
		$N''_{exp.}$ (10^{-4} kg/m² s)	$N''_{theo.}$ (10^{-4} kg/m² s)	Error%	$N''_{exp.}$ (10^{-4} kg/m² s)	$N''_{theo.}$ (10^{-4} kg/m² s)	Error%	$N''_{exp.}$ (10^{-4} kg/m² s)	$N''_{theo.}$ (10^{-4} kg/m² s)	Error%	$N''_{exp.}$ (10^{-4} kg/m² s)	$N''_{theo.}$ (10^{-4} kg/m² s)	Error%	$N''_{exp.}$ (10^{-4} kg/m² s)	$N''_{theo.}$ (10^{-4} kg/m² s)	Error%
50	0.3	5.39	5.92	8.89	7.18	6.80	5.33	6.19	6.70	7.57	6.07	6.61	8.16	5.99	6.53	8.25
	0.5	6.42	6.82	5.90	7.79	8.00	2.64	7.48	7.90	5.24	7.34	7.79	5.79	7.14	7.71	7.38
	0.7	7.42	7.74	4.08	9.69	9.36	3.54	9.53	9.20	3.53	9.49	9.07	4.63	9.31	8.95	4.04
	0.9	8.52	8.36	1.97	11.12	10.32	7.22	10.46	10.14	3.19	9.69	9.98	2.87	9.34	9.85	5.19
50	0.3	6.88	7.49	8.16	7.95	8.69	8.49	7.82	8.56	8.68	7.65	8.43	9.34	7.59	8.34	9.02
	0.5	8.22	9.01	8.77	11.24	10.67	5.14	10.33	10.51	1.73	9.90	10.38	4.57	10.38	10.23	1.41
	0.7	9.77	10.30	5.18	13.13	12.54	4.47	12.41	12.34	0.57	12.33	12.17	1.29	11.69	12.00	2.58
	0.9	11.45	11.10	3.16	14.28	13.96	2.26	13.41	13.63	1.62	12.83	13.36	3.93	12.54	13.15	4.62
55	0.3	8.71	9.61	9.32	10.46	11.30	7.38	10.21	11.13	8.27	10.36	10.96	5.48	10.13	10.81	6.27
	0.5	10.63	11.40	6.72	14.28	13.60	5.07	12.87	13.41	4.03	12.84	13.26	3.22	11.97	13.09	8.58
	0.7	12.65	13.00	2.70	16.25	16.04	1.28	15.94	15.78	1.05	14.82	15.54	4.63	13.97	15.31	8.75
	0.9	14.68	14.15	3.75	18.46	17.96	2.74	18.00	17.62	2.16	17.56	17.27	1.72	16.17	16.99	4.84
60	0.3	10.86	11.88	8.59	13.61	14.05	3.15	13.12	13.86	5.39	12.75	13.73	7.14	12.35	13.61	9.26
	0.5	13.38	14.09	5.02	15.68	17.14	8.56	15.52	16.87	7.97	15.34	16.59	7.52	15.14	16.36	7.42
	0.7	15.76	15.94	1.10	20.75	19.88	4.19	19.87	19.57	1.48	19.34	19.27	0.37	19.10	18.97	0.69
	0.9	18.15	17.30	4.92	22.64	22.22	1.87	22.44	21.78	2.92	22.15	21.44	3.28	21.69	21.14	2.53

Table 2(b)
Comparison of theoretical and experimental permeates flux of various operation conditions and channel design for countercurrent-flow operations

$T_{h,in}$ (°C)	Q (L/min)	Empty channel			Carbon-fiber channel											
					2 mm, 90°			2 mm, 120°			3 mm, 90°			3 mm, 120°		
		$N''_{exp.}$ (10^{-4} kg/m² s)	$N''_{theo.}$ (10^{-4} kg/m² s)	Error%	$N''_{exp.}$ (10^{-4} kg/m² s)	$N''_{theo.}$ (10^{-4} kg/m² s)	Error%	$N''_{exp.}$ (10^{-4} kg/m² s)	$N''_{theo.}$ (10^{-4} kg/m² s)	Error%	$N''_{exp.}$ (10^{-4} kg/m² s)	$N''_{theo.}$ (10^{-4} kg/m² s)	Error%	$N''_{exp.}$ (10^{-4} kg/m² s)	$N''_{theo.}$ (10^{-4} kg/m² s)	Error%
50	0.3	6.03	6.64	9.23	8.33	7.79	6.47	7.02	7.66	8.31	6.89	7.54	8.57	6.84	7.41	7.72
	0.5	7.27	7.44	2.33	8.42	8.88	5.19	8.40	8.76	4.04	8.10	8.65	6.35	7.87	8.51	7.46
	0.7	8.13	8.27	1.74	10.49	10.15	3.21	10.32	10.01	3.09	9.35	9.89	5.52	10.03	9.74	2.83
	0.9	9.19	8.87	3.53	11.61	11.31	2.55	10.78	11.07	2.62	10.48	10.88	3.63	10.25	10.67	3.96
50	0.3	7.84	8.68	9.66	9.52	10.28	7.43	9.33	10.09	7.58	9.00	9.91	9.16	8.81	9.76	9.74
	0.5	9.08	10.04	9.53	12.59	12.18	3.27	11.33	11.99	5.44	11.18	11.79	5.14	10.95	11.61	5.73
	0.7	10.72	11.19	4.14	14.49	14.04	3.12	14.13	13.76	2.71	13.96	13.52	3.27	13.78	13.29	3.57
	0.9	12.35	11.78	4.83	16.12	15.27	5.30	15.46	14.89	3.85	15.22	14.58	4.39	14.85	14.32	3.62
55	0.3	10.24	11.27	9.16	12.29	13.55	9.28	12.15	13.33	8.86	12.01	13.11	8.43	11.81	12.91	8.53
	0.5	11.93	12.91	7.54	15.45	15.88	2.71	14.87	15.61	4.75	14.74	15.39	4.26	14.57	15.15	3.82
	0.7	13.83	14.15	2.31	18.30	18.01	1.54	17.86	17.67	1.06	17.06	17.39	1.88	16.91	17.09	1.04
	0.9	16.13	15.10	6.84	21.04	20.06	4.66	19.95	19.51	2.23	19.51	19.02	2.61	19.07	18.61	2.39
60	0.3	12.92	13.94	7.32	16.15	17.05	5.29	15.95	16.75	4.81	15.52	16.50	5.94	15.07	16.23	7.12
	0.5	14.84	15.82	6.18	19.94	19.89	0.25	18.75	19.45	3.62	18.09	19.12	5.37	17.72	18.80	5.77
	0.7	17.46	17.35	0.59	22.88	22.51	1.62	22.35	22.00	1.57	21.60	21.48	0.56	20.94	21.12	0.85
	0.9	19.89	18.74	6.10	25.88	25.15	2.83	24.99	24.49	2.04	24.73	23.97	3.18	24.27	23.46	3.32

Table 3(a)
Effects of operation conditions and channel design on I_N and TPC for concurrent-flow operations

$T_{h,in}$ (°C)	Q (L/min)	Empty channel		Carbon-fiber channel					
				2 mm			3 mm		
		N'' (10^{-4} kg/m^2 s)	TPC	N'' (10^{-4} kg/m^2 s)	I_N(%)	TPC	N'' (10^{-4} kg/m^2 s)	I_N(%)	TPC
45	0.3	5.92	0.3015	6.80	14.84	0.4018	6.53	10.26	0.3856
	0.5	6.82	0.3073	8.00	17.33	0.4176	7.71	13.07	0.4007
	0.7	7.74	0.3194	9.36	20.87	0.4322	8.95	15.67	0.4147
	0.9	8.36	0.3245	10.32	24.47	0.4454	9.85	17.82	0.4275
50	0.3	7.49	0.2934	8.69	15.61	0.3923	8.34	11.32	0.3764
	0.5	9.01	0.2970	10.67	18.33	0.4068	10.23	13.64	0.3903
	0.7	10.30	0.3023	12.54	21.74	0.4196	12.00	16.52	0.4026
	0.9	11.10	0.3094	13.96	25.73	0.4332	13.15	18.47	0.4157
55	0.3	9.61	0.2679	11.30	16.72	0.3686	10.81	12.57	0.3537
	0.5	11.40	0.2751	13.60	19.26	0.3863	13.09	14.86	0.3708
	0.7	13.00	0.2799	16.04	23.38	0.3987	15.31	17.76	0.3826
	0.9	14.15	0.2850	17.96	27.59	0.4118	16.99	20.13	0.3952
60	0.3	11.88	0.2599	14.05	18.04	0.3493	13.61	14.51	0.3352
	0.5	14.09	0.2632	17.14	21.67	0.3610	16.36	16.08	0.3465
	0.7	15.94	0.2695	19.88	24.73	0.3707	18.97	19.04	0.3558
	0.9	17.30	0.2740	22.22	28.42	0.3845	21.14	22.21	0.3689

Note: TPC data are the average value of the entire DCMD module.

$$\ell w_{f,i} = \frac{2 f_{F,i} \overline{v}_i^2 L}{De_i}, i = h, c \tag{18}$$

in which:

$$\overline{v}_h = \frac{Q}{\left[dW - d'\left(n_{1,h} w_{1,h} + n_2 w_2\right)\right]}, \overline{v}_c = \frac{Q}{\left(dW - n_{1,c} d' w_{1,c}\right)} \tag{19}$$

$$De_{h,h} = \frac{4\left[dW - d'\left(n_{1,h} w_{1,h} + n_2 w_2\right)\right]}{2\left(d + W + n_{1,c} d' + n_{2,} d'\right)}, De_{h,c} = \frac{4\left(dW - n_{1,c} d' w_{1,c}\right)}{2\left(d + W + n_{1,c} d'\right)} \tag{20}$$

The Fanning friction factor can be estimated using a correlation based on the aspect ratio of the channel (β = d/W) [25]:

$$f_F = \frac{C}{\mathrm{Re}} \tag{21}$$

$$C = 24\left(1 - 1.3553\beta + 1.9467\beta^2 - 1.7012\beta^3 + 0.9564\beta^4 - 0.2537\beta^5\right) \tag{22}$$

For discussion of the relative degree of flux enhancement and power consumption increase, the relative index I_N and I_P are defined. Their definitions are:

$$I_N = \frac{N_s'' - N_n''}{N_n''} \tag{23}$$

$$I_P = \frac{P_s - P_n}{P_n} \tag{24}$$

where the subscripts s and n represents the channels with inserting W-shaped carbon-fiber spacers and the empty channels.

3. Experimental setup

The schematic representations of the DCMD module for both concurrent- and countercurrent-flow operations are illustrated in Fig. 2, respectively. The outside walls of the entire module are acrylic plates while the hot-fluid channels and cold-fluid channels are stacked together with inserting W-shaped carbon-fiber spacers into the hot-fluid acrylic plate and serving as turbulence promoters. One 1-mm thick W-shaped carbon-fiber spacers is placed on the hot stream side of the hydrophobic membrane with various hydrodynamic angles. The acrylic plate has three holes for the fluid-distribution flowing in and out at both entrance and exit ends, respectively. The experimental system of the DCMD unit with inserting W-shaped carbon-fiber spacers is illustrated in Fig. 3.

Detail design of the W-shaped carbon-fiber spacers is displayed in Fig. 4 where 2 and 3 mm of open slot and 90° and 120° of hydrodynamic angle of the spacers were tested in this study. The 1-mm thick carbon-fiber sheet was implemented as a support in the cold-fluid channel. Between the W-shaped carbon-fiber spacer and the acrylic plate is a

Table 3(b)
Effects of operation conditions and channel design on I_N and TPC for countercurrent-flow operations

$T_{h,in}$ (°C)	Q (L/min)	Empty channel		Carbon-fiber channel					
				2 mm			3 mm		
		N'' (10^{-4} kg/m^2 s)	TPC	N'' (10^{-4} kg/m^2 s)	I_N (%)	TPC	N'' (10^{-4} kg/m^2 s)	I_N (%)	TPC
45	0.3	6.64	0.3186	7.79	17.27	0.4141	7.41	11.62	0.3974
	0.5	7.44	0.3248	8.88	19.24	0.4299	8.51	14.26	0.4126
	0.7	8.27	0.3375	10.15	22.73	0.4450	9.74	17.82	0.4270
	0.9	8.87	0.3429	11.31	27.49	0.4586	10.67	20.31	0.4401
50	0.3	8.68	0.3012	10.28	18.51	0.4034	9.76	12.55	0.3871
	0.5	10.04	0.3048	12.18	21.36	0.4175	11.61	15.66	0.4006
	0.7	11.19	0.3103	14.04	25.48	0.4320	13.29	18.79	0.4145
	0.9	11.78	0.3177	15.27	29.58	0.4456	14.32	21.48	0.4276
55	0.3	11.27	0.2830	13.55	20.17	0.3793	12.91	14.52	0.3640
	0.5	12.91	0.2909	15.88	23.02	0.3974	15.15	17.38	0.3813
	0.7	14.15	0.2957	18.01	27.28	0.4094	17.09	20.72	0.3929
	0.9	15.10	0.3012	20.06	32.84	0.4235	18.61	23.25	0.4064
60	0.3	13.94	0.2667	17.05	22.36	0.3693	16.23	16.45	0.3544
	0.5	15.82	0.2703	19.89	25.73	0.3817	18.80	18.84	0.3663
	0.7	17.35	0.2758	22.51	29.68	0.3919	21.12	21.69	0.3761
	0.9	18.74	0.2818	25.15	34.17	0.4064	23.46	25.17	0.3904

Note: TPC data are the average value of the entire DCMD module.

1-mm thick silicon rubber sealing to prevent leakage as well as to serve as part of the flow channel thickness. The length, width, and height of each hot and cold channel are 0.21 m, 0.29 m, and 2 mm, respectively. The hydrophobic polytetrafluoroethylene membrane (ADVANTEC, Tokyo, Japan) with a nominal pore size of 0.1 mm, a porosity of 0.72, and a thickness of 130 mm was used.

The hot inlet saline water of 3.5 wt% NaCl was prepared using distilled water and conducted for various inlet hot-fluid temperatures (45°C, 50°C, 55°C, and 60°C) with flow rate variations (0.3, 0.5, 0.7, and 0.9 L/min) while the cold fluid had a fixed inlet temperature of 25°C but its volumetric flow rate was the same as the hot fluid. Two thermostats were used to keep the inlet hot and cold fluids at specified temperatures. The permeate flux condensed at the cold channel, which was collected and weighted using an electronic balance.

4. Results and discussion

The temperature distributions inside the DCMD module can be solved numerically using the theoretical model. The temperature profiles presented in Fig. 5 show that the membrane surface temperatures and the fluid temperatures of channels with and without (empty channel) W-shaped carbon-fiber spacer are notably different for both concurrent and countercurrent flows. The temperature gradient between both sides of the membrane is higher in channels with carbon-fiber spacers than that in the empty channel as listed in Tables 1(a) and (b). The increased temperature gradient results in more heat flux in the channel with carbon-fiber spacers, hence, more distillate flux or pure water productivity was predicted. When compared the temperature gradient between both sides of the membrane for the 2 and 3 mm slot opening of carbon-fiber spacers, one finds temperature gradient of the 2 mm slot is higher than that of the 3 mm slot. That results in a higher heat transfer and permeate flux will be elucidated later. Contrast to the uniform temperature gradient along the channel of the countercurrent flow, the temperature gradient appears a non-uniform distribution and is comparatively higher in the entrance and lower in the outlet for the concurrent flow. In the concurrent flow operation, as the salinity in the hot feed side is increased along the channel due to loss of pure water that reduces water activity coefficient of the hot stream, therefore, the saturation pressure of the hot side is reduced that also reduces the pressure gradient across the membrane. The descending heat transfer and permeate flux along the channel for concurrent flow operation is thus expected.

The theoretical predictions of temperature distributions could allow the determination of TPC, as shown in Fig. 6. The higher inlet saline temperature results in the lower TPC for both concurrent- and countercurrent-flow operations. This is due to the higher inlet saline temperature produces the more permeate flux resulting the lower temperature difference across the membrane surfaces. Restated, the higher inlet saline temperature

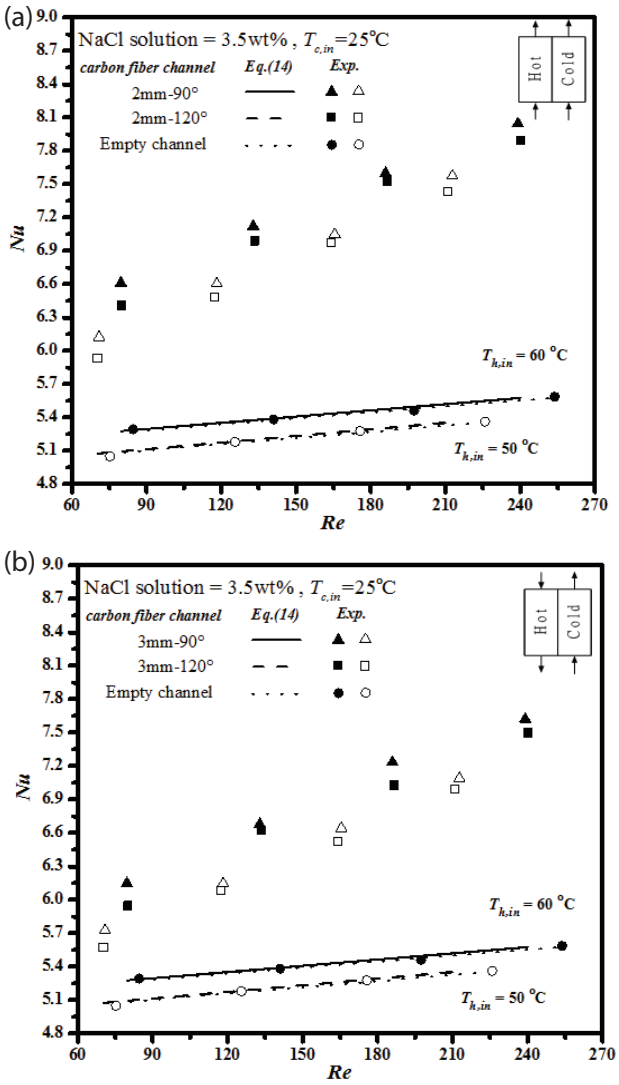

Fig. 8. Dependence of Nu on Re (solid symbols: 60°C, open symbols: 50°C). (a) Concurrent-flow operations and (b) countercurrent-flow operations.

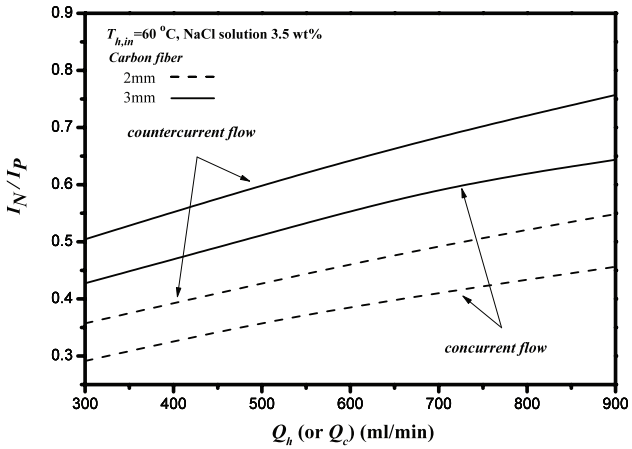

Fig. 9. Effect of flow type, slot opening of spacer and flow rate on energy consumption increment.

creates a higher temperature difference of $(T_h - T_c)$ than that of $(T_2 - T_1)$, so that a lower TPC = $(T_2 - T_1)/(T_h - T_c)$ was obtained. The inserted W-shaped carbon-fiber spacer results in a higher TPC was found when comparing the TPC of the carbon-fiber spacer of 2 and 3 mm slot opening with that of the empty channel as shown in Fig. 6. The inserted carbon-fiber spacer disturbs the thermal boundary layer on the membrane surface, thus more heat transfer efficiency achieved and less temperature polarization or higher TPC was found. Comparing the overall TPC value of the concurrent- and countercurrent-flow operation along the channel, a higher TPC value was achieved in the countercurrent-flow operation than that in the concurrent-flow operation. The countercurrent-flow operation gives a higher TPC value than that of the concurrent-flow operation, as indicated in Figs. 6(a) and (b) and Tables 3(a) and (b) as well. The effect of the extent of TPC improvement is more significant in countercurrent-flow configurations, and thus, the reduction of the temperature gradient between the bulk stream and membrane surface with the less thermal resistance is achieved.

The theoretical predictions and experimental results of permeate flux were presented graphically in Fig. 7 for the empty channel and the channels with 2 and 3 mm inserting W-shaped carbon-fiber spacers, respectively. The agreement between the experimental results and theoretical predictions are fairly good, as indicated in Tables 2(a) and (b) where the errors are within acceptable range. The results of how permeate flux varies with volumetric flow rates, hot saline inlet temperatures, with and without inserting carbon-fiber spacers in both concurrent- and countercurrent-flow operations of the DCMD system can be concluded as follows:

- The permeate flux increases with the increase of the volumetric flow rate.
- The higher the inlet saline temperature results in the higher distillate flux or pure water productivity.
- The permeate flux enhancement is obtained with inserting the W-shaped carbon-fiber spacers where the enhancement of the 2 mm slot opening is higher than that of the 3 mm.
- The permeate flux of the 90° hydrodynamic angle in the slot of the carbon-fiber spacers is higher than that of the 120°.

The permeate flux increases with increasing the volumetric flow rate is due to enhancing the convective heat-transfer of the hot feed stream, and thus, the thinner thermal boundary layer with a lower thermal resistance and a larger TPC were achieved. Consequently, the reduction of the boundary layer thickness provides a larger vapor pressure gradient which results in a higher permeate flux through the hydrophobic membrane. The permeate flux enhancement with the use of the turbulence promoter by inserting W-shaped carbon-fiber spacers is significantly as illustrated in Figs. 7(a) and (b). Notice that the effect of hydrodynamic angle on the permeate flux concludes that more permeate flux was found in the 90° of the spacers than that of the 120°.

Table 4
Effect of operation conditions and channel design on permeate flux N'' and flux enhancement index I_N for concurrent- and countercurrent-flow operations

Concurrent-flow		Empty channel	W-shaped carbon-fiber channel							
			2 mm, 90°		2 mm, 120°		3 mm, 90°		3 mm, 120°	
$T_{h,in}$ (°C)	Q (L/min)	N'' (10^{-4} kg/m^2 s)	N'' (10^{-4} kg/m^2 s)	I_N(%)	N'' (10^{-4} kg/m^2 s)	I_N(%)	N'' (10^{-4} kg/m^2 s)	I_N(%)	N'' (10^{-4} kg/m^2 s)	I_N(%)
50	0.3	7.49	8.69	15.61	8.56	14.26	8.43	12.53	8.34	11.32
	0.5	9.01	10.67	18.33	10.51	16.71	10.38	15.21	10.23	13.64
	0.7	10.30	12.54	21.74	12.34	19.83	12.17	18.19	12.00	16.52
	0.9	11.10	13.96	25.73	13.63	22.79	13.36	20.34	13.15	18.47
60	0.3	11.88	14.05	18.04	13.86	16.66	13.73	15.58	13.61	14.51
	0.5	14.09	17.14	21.67	16.87	19.71	16.59	17.75	16.36	16.08
	0.7	15.94	19.88	24.73	19.57	22.82	19.27	20.89	18.97	19.04
	0.9	17.30	22.22	28.42	21.78	25.92	21.44	23.95	21.14	22.21
Countercurrent-flow			2 mm, 90°		2 mm, 120°		3 mm, 90°		3 mm, 120°	
50	0.3	8.68	10.28	18.51	10.09	16.34	9.91	14.26	9.76	12.55
	0.5	10.04	12.18	21.36	11.99	19.39	11.79	17.45	11.61	15.66
	0.7	11.19	14.04	25.48	13.76	22.96	13.52	20.86	13.29	18.79
	0.9	11.78	15.27	29.58	14.89	26.34	14.58	23.72	14.32	21.48
60	0.3	13.94	17.05	22.36	16.75	20.23	16.50	18.39	16.23	16.45
	0.5	15.82	19.89	25.73	19.45	22.95	19.12	20.82	18.80	18.84
	0.7	17.35	22.51	29.68	22.00	26.76	21.48	23.78	21.12	21.69
	0.9	18.74	25.15	34.17	24.49	30.63	23.97	27.88	23.46	25.17

However, the difference between the two results is insignificant. The considerable increment of permeate flux by using W-shaped carbon-fiber spacers is obvious for the high hot-fluid inlet temperature operation and the results is consistent with previous study [15]. The results show that the W-shaped carbon-fiber channels could enhance the heat transfer coefficient, and up to 34% pure water flux increment is thus obtained.

The dependence of Nusselt number (Nu) on Reynolds number (Re) is illustrated in Fig. 8 where the Nu increased with the increasing Re. Notice that the effect of inserting carbon-fiber spacer significantly increases the Nu or convective heat transfer for both 2 and 3 mm slot opening of the spacers. Contrast to the considerable effect by the spacer slot opening, the hydrodynamic angle of the spacer changes from 90° to 120° plays less effect on the variation of Nu for both concurrent- and countercurrent-flow operations. When comparing the Nusselt number (Nu) of the empty channel with that of the channel with 2 or 3 mm spacer in Fig. 8, one found a 20% overall increase in Nusselt number resulting from the inserting W-shaped carbon-fiber spacers. Hence, the enhancement factor for predicting the Nusselt number for the device with W-shaped carbon-fiber spacers was obtained in Eq. (15). The experimental results of N'', TPC, and I_N for concurrent- and countercurrent-flow operations are summarized in Tables 3(a) and (b). The selected data of how the operation conditions and channel design of slot openings and the effects of hydrodynamic angles on permeate flux N'' and flux enhancement index I_N are also listed in Table 4. The effects of flow configuration, slot opening dimension, and flow rate on I_N/I_P are shown in Fig. 9. The increase of flow rate gives higher value of I_N/I_P, which indicates the expenses of energy consumption is more effective in increasing the permeate flux. The value of I_N/I_P in countercurrent-flow configuration is higher than that in concurrent-flow configuration. It is because the countercurrent-flow operation utilizes the temperature driving force more effectively. The I_N/I_P of the channel with 2 mm slot opening of the spacer is higher than the channel with 3 mm slot opening. Although the Nusselt number and permeate flux of the channel with 3 mm open slot are both higher, the power consumption is also higher. The effective utilization of power consumption, in terms of I_N/I_P, is higher when the channel with 2 mm slot opening spacer is used. Summarizing the effects of inserting W-shaped carbon-fiber spacers, one can conclude that a higher value of I_N/I_P, as shown in Fig. 9, which means the permeate flux improvement is more effective at the expense of energy consumption.

5. Conclusions

The turbulence promoter of flow channel in DCMD system was implemented by inserting W-shaped carbon-fiber spacers and was developed mathematically considering both the heat and mass transfer of each layer of the module and verified by experimental data. Experimental study has demonstrated its feasibility and up to 34% of permeate flux enhancement was obtained by the inserting W-shaped carbon-fiber spacers with 2 mm slot opening of the spacer and 90° of hydrodynamic angle setup in the DCMD system. The mathematical treatments in aiming to predict temperature distributions and pure water productivity were presented graphically with the volumetric flow rates, inlet saline temperatures, and hydrodynamic angles as parameters in concurrent- and countercurrent-flow operations. The effects of the W-shaped carbon-fiber spacers on the desalination performance and energy consumption were presented. Both theoretical and experimental data conclude that the flow channel using the W-shaped carbon-fiber spacers gives higher permeate flux than the one with empty channel; however, the effective utilization of power consumption of the former is comparatively higher.

Symbols

a_w — Water activity in NaCl solution
C — Friction losses coefficient in Eq. (21)
c_K — Membrane coefficient based on the Knudsen diffusion model, kg/(m²·Pa·s)
c_m — Membrane permeation coefficient, kg/(m²·Pa·s)
c_M — Membrane coefficient based on the molecular diffusion model, kg/(m²·Pa·s)
C_P — Heat capacity, J/(kg·K)
d — Channel height, m
d' — Carbon-fiber height, m
De — Equivalent hydraulic diameter of channel, m
De_f — Hydraulic diameter of the empty channel, m
D_m — Diffusion coefficient of air and vapor in the membrane, m²/s
f_F — Friction factor
h — Convection coefficient, W/(m² K)
I_N — Permeate flux relative factor, defined by Eq. (23)
I_P — Power consumption relative index, defined by Eq. (24)
k — Thermal conductivity coefficient of the fluid, J/(s·m·K)
k_g — Thermal conductivity of gas, J/(s·m·K)
k_m — Thermal conductivity of membrane, J/(s·m·K)
k_s — Thermal conductivity of solid membrane, J/(s·m·K)
L — Channel length, m
lw_f — Friction loss, J/kg
M_w — Molecular weight of water, kg/mol
$\dot{m}$ — Mass flow rate, kg/s
n_1 — Number of carbon-fiber
n_2 — Number of carbon-fiber fins
N'' — Distillate flux, kg/(m²·s)
Nu — Nusselt number
P — Pressure, Pa
P_c — Hydraulic friction loss of the cold fluid, W
P_h — Hydraulic friction loss of the hot fluid, W
P_{lost} — Hydraulic dissipate energy, W
P_n — Hydraulic friction loss of the fluid on the empty channel, W
P_r — Prandtl number
P_s — Hydraulic friction loss of the fluid in the channels with inserting W-shaped carbon-fiber spacers, W
P^{sat} — Saturation vapor pressure, Pa
P_2^{sat} — Saturation vapor pressure of membrane surface, Pa
q — Heat transfer rate, W/m²
q_c — Heat transfer rate between membrane surface and cold fluid, W/m²
q_h — Heat transfer rate between hot fluid and membrane surface, W/m²
q_m — Heat transfer rate between membrane surfaces, W/m²
Q — Volumetric flow rate, m³/s
R — Gas constant, J/(mol K)
Re — Reynolds number
r_p — Membrane pore radius, m
T — Temperature, °C
T_m — Mean temperature in membrane, °C
TPC — Temperature polarization coefficient
$\overline{v}$ — Average velocity, m/s
w_1 — Vertical carbon-fiber fin width, m
w_2 — Hypotenuse carbon-fiber fin width, $w_2 = W_e/\cos(\theta/2)$, m
W — Width of channel, m
W_e — Fin width of carbon-fiber, m
x_w — Liquid mole fraction of water
x_{NaCl} — Mole fraction of NaCl in saline solution
$|Y|_{\text{ln}}$ — Natural log mean mole fraction of air
y_w — Vapor mole fraction of water
z — Axial coordinate along the flow direction, m

Greek

α^E — Heat transfer enhancement factor
β — Dimensionless thickness, defined in Eq. (22)
δ_m — Thickness of membrane, m
ε — Membrane porosity
λ — Latent heat of water, J/kg
θ — Angle of carbon-fiber fin
ρ — Density, kg/m³
τ — Membrane tortuosity

Subscripts

1 — Membrane surface on cold-fluid side
2 — Membrane surface on hot-fluid side
c — Cold fluid
f — Reference scale
h — Hot fluid
exp. — Experimental
in — Inlet
lam — Laminar
n — Inserting nylon fiber as supporters
out — Outlet
s — Inserting carbon-fiber separators as supporters
theo. — Theoretical

Acknowledgment

The authors wish to thank the Ministry of Science and Technology of the Republic of China (Taiwan) for the financial support.

References

[1] O. Miyatake, H. Iwashita, Laminar-flow heat transfer to a fluid flowing axially between cylinders with a uniform wall heat flux, Int. J. Heat Mass Transfer, 34 (1991) 322–327.
[2] K.W. Lawson, D.R. Lloyd, Membrane distillation. II. Direct contact MD, J. Membr. Sci., 120 (1996) 123–133.
[3] A. Alkhudhiri, N. Darwish, N. Hilal, Treatment of saline solutions using air gap membrane distillation: experimental study, Desalination, 323 (2013) 2–7.
[4] U. Dehesa-Carrasco, C.A. Perez-Rabago, C.A. Arancibia-Bulnes, Experimental evaluation and modeling of internal temperatures in an air gap membrane distillation unit, Desalination, 326 (2013) 47–54.
[5] M. Essalhi, M. Khayet, Application of a porous composite hydrophobic/hydrophilic membrane in desalination by air gap and liquid gap membrane distillation: a comparative study, Sep. Purif. Technol., 133 (2014) 176–186.
[6] E. Drioli, A. Ali, F. Macedonio, Membrane distillation: recent developments and perspectives, Desalination, 356 (2015) 56–84.
[7] S. Devi, P. Ray, K. Singh, P.S. Singh., Preparation and characterization of highly micro-porous PVDF membranes for desalination of saline water through vacuum membrane distillation, Desalination, 346 (2014) 9–18.
[8] X. Huang, W.P. Wang, Y.D. Liu, H. Wang, Z.B. Zhang, W.L. Fan, L. Li., Treatment of oily waste water by PVP grafted PVDF ultrafiltration membranes, Chem. Eng. J., 273 (2015) 421–429.
[9] W. Kujawski, A. Sobolewska, K. Jarzynka, C. Güell, M. Ferrandob, J. Warczok, Application of osmotic membrane distillation process in red grape juice concentration, J. Food Eng., 116 (2013) 801–808.
[10] K.W. Lawson, D.R. Lloyd, Membrane distillation, J. Membr. Sci., 124 (1997) 1–25.
[11] M. Gryta, M. Tomaszewska, J. Grzechulska, A.W. Morawski, Membrane distillation of NaCl solution containing natural organic matter, J. Membr. Sci., 181 (2001) 279–287.
[12] T. Wang, Z. Zhang, X. Ren, L. Qin, D. Zheng, J. Li, Direct observation of single- and two-phase flows in spacer filled membrane modules, Sep. Purif. Technol., 125 (2014) 275–283.
[13] C.D. Ho, H. Chang, C.L. Chang, C.H. Huang, Theoretical and experimental studies of flux enhancement with roughened surface in direct contact membrane distillation desalination, J. Membr. Sci., 433 (2013) 160–166.
[14] M. Khayet, Membranes and theoretical modeling of membrane distillation: a review, Adv. Colloid Interface Sci., 164 (2011) 56–88.
[15] J.G. Lee, Y.D. Kim, W.S. Kim, L. Francis, G. Amy, N. Ghaffour, Performance modeling of direct contact membrane distillation (DCMD) seawater desalination process using a commercial composite membrane, J. Membr. Sci., 478 (2015) 85–95.
[16] R.W. Schofield, A.G. Fane, C.J.D. Fell, Heat and mass transfer in membrane distillation, J. Membr. Sci., 33 (1987) 299–313.
[17] L. Martínez-Díez, M.I. Vázquez-González, Effects of polarization on mass transport through hydrophobic porous membranes, Ind. Eng. Chem. Res., 37 (1998) 4128–4135.
[18] M.M. Teoh, S. Bonyadi, T.-S. Chung, Investigation of different hollow fiber module designs for flux enhancement in the membrane distillation process, J. Membr. Sci., 311 (2008) 371–379.
[19] X. Yang, H. Yu, R. Wang, A.G. Fane, Analysis of the effect of turbulence promoters in hollow fiber membrane distillation modules by computational fluid dynamic (CFD) simulations, J. Membr. Sci., 415–416 (2012) 758–769.
[20] S.B. Warner, Fiber Science, Princeton-Hall, Englewood Cliffs, NJ, 1995.
[21] H. Geng, H. Wu, P. Li, Q. He, Study on a new air-gap membrane distillation module for distillation, Desalination, 334 (2014) 29–38.
[22] R.W. Schofield, A.G. Fane, C.J.D. Fell, Gas and vapor transport through microporous membranes. I. Knudsen-Poiseuille transition, J. Membr. Sci., 53 (1990) 159–171.
[23] S.B. Iversen, V.K. Bhatia, K. Dam-Jphasen, G. Jonsson, Characterization of microporous membranes for use in membrane contactors, J. Membr. Sci., 130 (1997) 205–217.
[24] J. Phattaranawik, R. Jiraratananon, A.G. Fane, Heat transport and membrane distillation coefficient in direct contact membrane distillation, J. Membr. Sci., 212 (2002) 177–193.
[25] S. Kakac, R.K. Shah, W. Aung, Handbook of Single-Phase Convective Heat Transfer, Wiley, New York, 1987.